

# Design Space Exploration of Lithium-Ion Battery Packs for Hybrid-Electric Regional Aircraft Applications

Anna Misley,\* Aaron Sergent,† Matilde D'Arpino,‡ Prashanth Ramesh,§ and Marcello Canova¶ *The Ohio State University, Columbus, Ohio 43210* 

https://doi.org/10.2514/1.B38658

Distributed hybrid and electric propulsion systems are one of the most promising technologies to reduce aircraft emissions, resulting in research efforts to investigate new architectures and the design of optimal energy management strategies. This work defines the optimal requirements in terms of battery pack sizing and cell technology for a hybrid-electric regional wing-mounted distributed propulsion aircraft through the application of a design space exploration method. The propulsion system considered in this study is a series-parallel hybrid turboelectric power train with distributed electric fans. A set of six lithium-ion battery cell technologies was identified and experimentally characterized, including both commercially available and prototype cells at different combinations of specific energy and power. A model of the aircraft was developed and used to define the optimal energy management strategy for the hybrid turboelectric propulsion system, which was solved using dynamic programming. The design space exploration was conducted by varying the cell technology and battery storage system size; and the effects on fuel consumption, energy management strategy, and thermal management were compared.

#### **Nomenclature**

specific heat,  $J/(kg \cdot K)$ 

drag force, N

battery voltage, V

aircraft speed, m/s

aircraft path angle, rad

state variable

time step, s

efficiency, %

torque, N/m

F	=	thrust
$f_p$	=	battery pack packaging factor
$\frac{g}{\bar{h}}$	=	gravitational acceleration, m/s <sup>2</sup>
$ar{h}$	=	altitude, m
I	=	current, A
J	=	objective function
k	=	index of time
M	=	Mach number
m	=	mass, kg
N	=	number of time discretization points
$N N_1$	=	number of time discretization points low-pressure compressor corrected rotational speed
		low-pressure compressor corrected rotational speed
$N_1$ $n$	=	low-pressure compressor corrected rotational speed ratio, $\%$
$N_1$ $n$	=	low-pressure compressor corrected rotational speed ratio, % number of units
$N_1$	= = =	low-pressure compressor corrected rotational speed ratio, % number of units power, W
$N_1$ $n$	= = =	low-pressure compressor corrected rotational speed ratio, % number of units power, W heat flux, W

## Subscripts

υ

 $\boldsymbol{x}$ 

γ

 $\Delta t$ 

η

a = aircraft

=

=

=

Received 27 September 2021; revision received 5 October 2022; accepted for publication 5 October 2022; published online 25 November 2022. Copyright © 2022 by the American Institute of Aeronautics and Astronautics, Inc. All rights reserved. All requests for copying and permission to reprint should be submitted to CCC at www.copyright.com; employ the eISSN 1533-3876 to initiate your request. See also AIAA Rights and Permissions www.aiaa.org/randp.

conv = converter cool = cooling

e = operating empty aircraft

f = fuel fan = fan

gen = generation or generator

inv = inverter lim = limits

p = payload or parallel

r = required
rec = rectifier
s = series
tot = total
ts = turboshaft

# I. Introduction

T HE need for carbon dioxide (CO2) emissions reduction and increasing fuel costs have been the main drivers for electrification in the aerospace industry, leading to the research into many different aspects related to electric aircraft design [1-4]. Several electrified architectures have been proposed for the propulsion system, ranging from fully electric to turboelectric and including distributed hybrid-electric propulsion systems [5–10]. In particular, hybrid-electric aircraft propulsion systems can be classified as parallel and series architectures. In the parallel hybrid configuration, the turbofan engine is coupled to an electric motor and inverter, powered by a battery pack. This requires fewer modifications to the conventional aircraft than for the series architecture. In series hybrid configurations, the propulsion is achieved by electric fans powered by turbogenerators and batteries. This configuration, also called hybrid turboelectric, requires a completely different architecture of the aircraft and an increase of the number of components, which increase the complexity and the weight. However, the series architecture enables the use of distributed electric propulsion, which is achieved by installing multiple electrically driven fans. Distributed propulsion has been proven to reduce aerodynamic drag, increase the bypass and pressure ratio of the propulsor, and reduce thrust specific fuel consumption with respect to traditional engines. This technology can potentially increase the system efficiency, modularity, and redundancy at the cost of weight and complexity [11–14].

The electrification of the aircraft propulsion system may allow for efficiency increases, which can reduce fuel consumption if the aircraft, propulsion system, and control strategy are optimized for the specific application [8,15–19]. However, it is important to note that

randp.

\*Postdoctoral Researcher, Department of Mechanical and Aerospace Engineering; misley.3@osu.edu.

<sup>†</sup>Graduate Student, Center for Automotive Research; sergent.27@osu.edu.
†Research Scientist, Center for Automotive Research; darpino.2@osu.edu.

\*\*Lead Engineer, Center for Automotive Research; ramesh.47@osu.edu.

<sup>&</sup>lt;sup>1</sup>Professor, Department of Mechanical and Aerospace Engineering; canova 1.@osu.edu.

BP = battery pack cell = cell

several studies considered highly optimistic values for the cell specific energy. Hybrid propulsion systems can lead to an increase in the overall weight and cost of the aircraft, requiring a careful design and sizing of the system to compromise between upfront cost increase and fuel reduction capabilities [20-23]. High specific power and high-efficiency electric machines, generators, and inverters are key technologies to enable hybrid-electric propulsion [24–27]. However, as the specific power increases, the complexity in the extraction of the generated heat requires advanced solutions for thermal management [28-31]. For hybrid-electric power trains, the design, sizing, and control of the battery energy storage system have relevant impact on the performance and fuel consumption of the aircraft and have to be determined for the specific application to achieve the aforementioned benefits [19,32,33]. Different sizing and selection of the electric propulsion system will require different strategies for energy management, and so it is important to include the control aspect in the propulsion system design process.

The development of optimal energy management strategies for hybrid propulsion systems has been largely studied in the past decades for ground vehicles [34–37]. However, the aviation sector appears more focused on the optimal sizing of the aircraft components rather than on the control of the power split. For this reason, many published design studies implemented strategies that assumed a constant power split or simple heuristic algorithm, whereas other studies attempted to divide the mission into smaller segments and apply a constant power split to each segment [38]. The more recent work done in Refs. [19,39,40] highlighted the correlation between the control strategy and design of the propulsion system [41–43]. Moreover, the importance of realistic battery models, calibrated using experimental data, is becoming an important aspect of research in the design and optimization of electrified propulsion systems.

Although different studies focused on the design and sizing of the hybrid propulsion system [44–46], there were limited studies that investigated the cooptimization of the propulsion system design and control for a hybrid aircraft propulsion system. To this end, this work presents a design optimization study for an electrified aircraft, which illustrates how the selection of specific lithium-ion battery cell technologies affects the fuel consumption as well as the power and thermal management strategy of the hybrid turboelectric propulsion system over a range of missions. For this study, a design space exploration is performed, which requires performing a cooptimization of the battery pack design, the power split control strategy for the

hybrid propulsion system, and the thermal management strategy of the battery pack.

Central to this work is the use of experimental data collected on six different cell technologies, covering both commercially available lithium-ion cells and next-generation technologies, characterized by different tradeoffs between specific power and specific energy. The design space exploration is performed for three different mission profiles of different lengths, ranging from 550 to 1850 km.

The study analyzes the interdependence of the control strategy and the thermal management strategy with the cell technology selection and design of the battery pack. In addition, this work provides insights on the fuel savings and system performance achievable by adopting different lithium-ion cell technologies, which can guide the design and sizing of high-efficiency and low-emission hybrid-electric aircrafts. The developed modeling approach and the provided results can be extended to different power train and airframe architectures.

The paper is organized as follows: Sec. II reports the description of the aircraft architecture; Sec. III describes the mathematical model used to perform this research; Sec. IV includes the details of the design space exploration method, including the definition of the optimal control problem for the energy management strategy; and lastly, Sec. V reports the results and discussions.

#### II. Aircraft Architecture

A series-parallel hybrid-electric architecture with distributed propulsion for a regional commercial jet is considered in this work, as shown in Fig. 1. The main propulsive thrust is generated by eight fans, with each coupled to an electric motor and an inverter. The power provided to the electric motors is generated by two turboshaft engines, with each including a free power turbine (FPT) coupled to a generator and a rectifier; and by a battery energy storage system (BESS), which includes the battery pack, a dc/dc converter, a battery management system, and a thermal management system (TMS). The turboshafts, in addition to producing electrical power, produce residual thrust.

The design of the baseline architecture and the component sizing was developed at Georgia Institute of Technology and described in Refs. [47,48]. The aircraft has been designed and sized as a pure turboelectric configuration for a design mission of 3660 km, 76 passengers, and a maximum takeoff mass  $m_{\rm MTOW}$  of 33,991 kg. This study is performed on the hybrid turboelectric configuration, which is

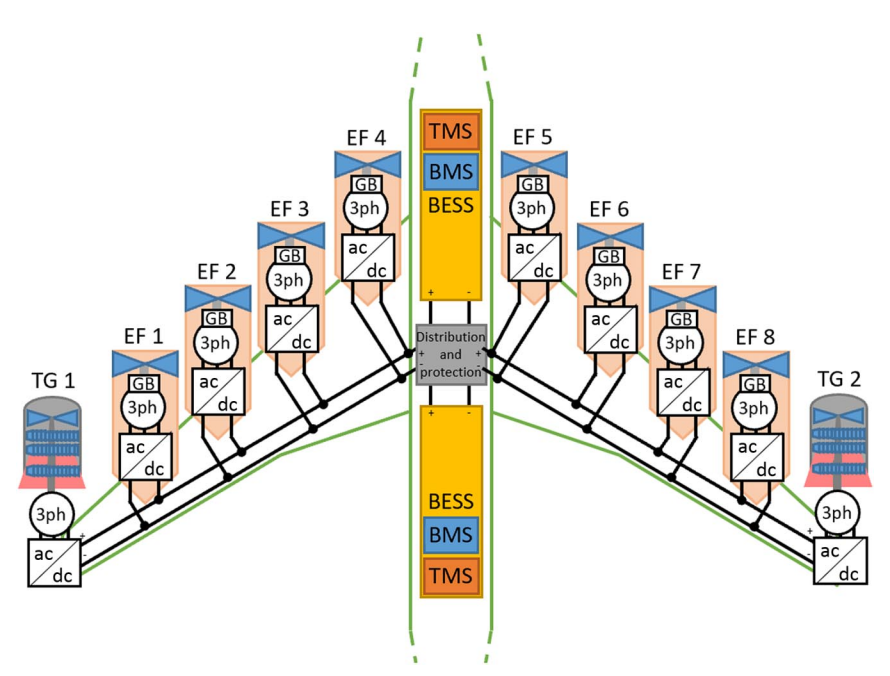


Fig. 1 Schematic of series-parallel hybrid turboelectric propulsion system architecture. Adapted from Ref. [19]. EF denotes electric fan, GB denotes gearbox, TG denotes turbogenerator, and 3ph denotes three-phase motor.

possible for shorter-range mission profiles when the aircraft mass does not reach the  $m_{\rm MTOW}$ . The hybrid configuration is obtained by adding reconfigurable battery modules to the floor of the aircraft. The battery TMS extracts bleed air from the turboshaft engines and directs it to the battery for cooling purposes. More details of the TMS can be found in Ref. [49].

# III. Model Description

Figure 2 shows a block diagram of the aircraft propulsion system model. The model inputs are the mission profile, which provides the operating conditions (altitude h and Mach number M) of the aircraft at each instant of time; and the control inputs [the engine low compressor corrected rotational speed ratio  $N_1$  and the cooling ratio (CR)] calculated by the energy management strategy. Because of the considered architecture,  $N_1$  controls the power generation at the turboshafts and indirectly controls the power split between the engine and the BESS power, whereas the CR controls the amount of cooling power directed to the battery. The outputs of the model are the power and thrust produced, the battery operating conditions (power, state of charge, current, voltage, and temperature), and the fuel burn. The model developed in MATLAB integrates a vehicle airframe model, which computes the thrust required to follow the desired mission profile; a model of the electric fans, which provides the main thrust for propulsion; a model of the turbogenerator, which converts the fuel energy into electrical energy for propulsion and produces residual thrust; and the BESS model, which calculates the electrical and thermal behavior. The model equations, developed in Ref. [19], are here summarized for clarity. The system and component parameters values used in the equations are summarized in Table A1 in the Appendix.

# A. Vehicle Airframe

The vehicle airframe model takes as inputs  $\bar{h}$  and M and calculates the thrust request  $F_r$ . Initially, the model calculates the total mass of the aircraft  $m_a$ :

$$m_a = m_e + m_p + m_{\text{BESS}} + m_f \tag{1}$$

assuming

$$\frac{dm_a}{dt} = \frac{dm_f}{dt} \tag{2}$$

where  $m_e$  is the operating empty mass of the aircraft,  $m_p$  is the payload,  $m_{\rm BESS}$  is the mass of the BESS, and  $m_f$  is the fuel mass. In this work,  $m_e$  and  $m_p$  are assumed to not change during the mission and have been set to a constant value determined in Ref. [47]. The fuel mass changes during the flight as the fuel is burned, whereas the BESS size is one of the parameters investigated in the design space exploration. The combined mass of the fuel and the BESS is limited to 7100 kg, which is defined by the maximum takeoff weight  $m_{\rm MTOW}$  [47].  $F_r$  is calculated by applying a force balance in the longitudinal and vertical directions, for which a small angle of attack is assumed [19]. The model and assumption chosen for the calculation result in

$$F_r = m_a v \dot{\gamma} + m_a g \sin \gamma + D \tag{3}$$

where v is speed of the aircraft, g is the gravitational acceleration,  $\gamma$  is the flight-path angle between the aircraft longitudinal axis and the horizon, and D is the drag force, which is calculated using a three-dimensional map of the drag coefficient. The drag coefficient map is a function of  $\bar{h}$ , M, and the lift coefficient and does not depend on thrust settings. The maps are extracted from a high-fidelity model of the aircraft developed with the software NPSS [47,50]. Assuming quasistatic conditions, the thrust required equals the thrust produced by the fans and the residual thrust produced by the turboshafts:

$$F_r = F_{\text{tot}} = F_{\text{TG}} + F_{\text{EF}} \tag{4}$$

where  $F_{\rm tot}$  is the total thrust production,  $F_{\rm TG}$  is the turbogenerator residual thrust, and  $F_{\rm EF}$  is the electric fan thrust.

### B. Turbogenerator

The turbogenerator model includes the turboshaft engine, the generator coupled to the FPT of the turboshaft, and the rectifier. The turboshaft data are extracted from the high-fidelity model described in Ref. [47]. The turboshaft model is based on three-dimensional maps; the dependent variables are the electrical power  $P_{\rm TG}$ , the residual thrust  $F_{\rm TG}$ , and the fuel mass flow rate  $\dot{m}_{f_{\rm tot}}$ ; whereas the independent variables are  $N_1$ ,  $\bar{h}$ , and M. The turboshaft model also provides the BESS cooling power  $\dot{Q}_{\rm cool}$  as bleed air extracted from the high-pressure compressor and redirected to the battery pack. The cooling power is computed from the CR, namely, as a fraction of the total turboshaft power produced:

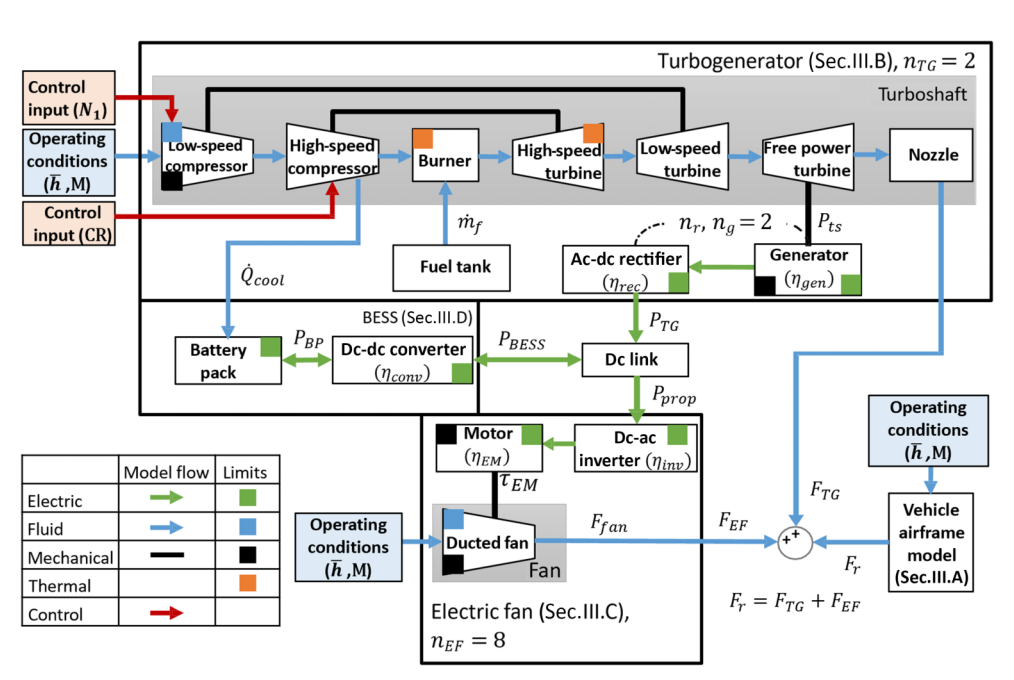


Fig. 2 Diagram of the model architecture of the series-parallel hybrid turboelectric propulsion system architecture.

$$\dot{Q}_{\text{cool}} = (\text{CR}) \sum_{i=0}^{n_{\text{TG}}} P_{\text{ts}_i}$$
 (5)

where  $n_{\rm TG}$  is the number of turbogenerators, and  $P_{\rm ts}$  is the power of the single turboshaft engine. The generator and rectifier are modeled as constant efficiency components with, respectively, 97.5 and 98.3% efficiencies [47,51,52]. The total residual thrust  $F_{\rm TG}$ , the total turbogenerator power  $P_{\rm TG}$ , and the total fuel mass flow rate  $\dot{m}_{f_{\rm tot}}$  are given by

$$\dot{m}_{f_{\text{tot}}} = \sum_{i=0}^{n_{\text{TG}}} \dot{m}_{f_i}(\bar{h}, M, N_1)$$
 (6)

$$F_{\text{TG}} = \sum_{i=0}^{n_{\text{TG}}} F_{\text{ts}_i}(\bar{h}, M, N_1)$$
 (7)

and

$$P_{\text{TG}} = \sum_{i=0}^{n_{\text{TG}}} P_{\text{ts}_i}(\bar{h}, M, N_1) (1 - \text{CR}) \eta_{\text{gen}} \eta_{\text{rec}}$$
 (8)

Note that the maps used in the model already account for the operating constraints as functions of the independent variables, whereas the limits on the CR are determined by the maximum bleed air mass flow rate [49]. This limits the CR to a maximum of 5%.

#### C. Electric Fan

The electric fan model calculates the thrust produced  $F_{\rm EF}$  and the power absorbed  $P_{\rm EF}$  by assuming constant efficiencies of 97.5% for the electric motor and 98.3% for the inverter [47,51,52]:

$$F_{\rm EF} = \sum_{i=0}^{n_{\rm EF}} F_{\rm fan_i}(\bar{h}, M, \tau_{\rm EM})$$
 (9)

$$P_{\rm EF} = \sum_{i=0}^{n_{\rm EF}} P_{{\rm fan}_i}(\bar{h}, M, \tau_{\rm EM}) \eta_{\rm EM} \eta_{\rm inv}$$
 (10)

where  $\tau_{\rm EM}$  and  $\eta_{\rm EM}$  are the electric motor torque and efficiency;  $\eta_{\rm inv}$  is the inverter efficiency;  $n_{\rm EF}$  is the number of electric fans; and  $F_{\rm fan}$  and  $P_{\rm fan}$  are the fan thrust and power, implemented as maps extracted from the high-fidelity model developed in NPSS [47,51,52]. The fan operating constraints are accounted for in the maps as functions of  $\bar{h}$ , M, and  $\tau_{\rm EM}$ ; whereas the motor and inverter constraints correspond to design values. The system and component parameters are listed in Table A1 in the Appendix.

#### D. Battery Energy Storage System

The BESS model includes the dc/dc converter and the battery pack. The BESS power request  $P_{\rm BESS}$  and the BESS cooling power  $\dot{Q}_{\rm cool}$  are inputs to the model. The BESS power request is obtained from a power balance at the dc link:

$$P_{\rm BESS} = P_{\rm EF} - P_{\rm TG} \tag{11}$$

The dc/dc converter is modeled with a constant efficiency (98.3%) and the cell behavior is assumed equal in all cells, which results in the calculation of cell power  $P_{\text{cell}}$ :

$$P_{\text{cell}} = \begin{cases} \frac{P_{\text{BP}}}{n_p n_s} = \frac{P_{\text{BESS}}}{\eta_{\text{conv}}} \frac{1}{n_p n_s}, & \text{if } P_{\text{BESS}} \ge 0\\ \frac{P_{\text{BP}}}{n_p n_s} = \frac{P_{\text{BESS}} \eta_{\text{conv}}}{n_p n_s}, & \text{if } P_{\text{BESS}} < 0 \end{cases}$$
(12)

where  $n_p$  is the number of cells in parallel, and  $n_s$  the number of cells in series [19]. A zeroth-order equivalent circuit model (ECM) has

been selected to represent the behavior of the cell and to predict the voltage (in volts), the state of charge (SOC), and the heat generation  $\dot{Q}_{\rm gen}$  of the battery by considering the power request and the temperature. The ECM used in this work is described by the following equations:

$$I = \frac{\text{OCV(SOC}, T_{\text{BP}}) - \sqrt{\text{OCV}^2(\text{SOC}, T_{\text{BP}}) - 4RP_{\text{cell}}}}{2R(\text{SOC}, T_{\text{RP}})}$$
(13)

$$V = OCV(SOC, T_{BP}) - R(SOC, T_{BP})I$$
 (14)

$$\dot{Q}_{\text{gen}} = (\text{OCV}(\text{SOC}, T_{\text{BP}}) - V)I \tag{15}$$

$$S\dot{O}C = -\frac{I}{C_{\text{corn}}} \tag{16}$$

where OCV is the open-circuit voltage, R is the internal resistance,  $C_{\rm nom}$  is the nominal capacity, and  $T_{\rm BP}$  the battery pack temperature [19]. The OCV and R maps have been determined experimentally and will be described in Sec. IV.A. The thermal model of the battery pack, assumed to be a lumped volume, calculates the temperature  $T_{\rm BP}$  as follows:

$$m_{\rm BP}c_{\rm BP}\frac{dT_{\rm BP}}{dt} = n_p n_s \dot{Q}_{\rm gen} - \dot{Q}_{\rm cool} \tag{17}$$

where  $m_{\rm BP}$  is the mass of the battery pack, and  $c_{\rm BP}$  is the heat capacity of the battery pack. The  $\dot{Q}_{\rm cool}$  is assumed to not depend on the cooling air temperature because it is calculated as a fraction of the turbogenerator power; see Eq. (5).

The model includes battery operation constraints, such as the SOC,  $T_{\rm BP}$ , V, I, and power limits; the latter is a function of the SOC and  $T_{\rm BP}$ . The cell constraints are listed in Sec. IV. Note that in this work, the cell-to-cell parameter variations have been ignored and the cell temperature is uniform, thanks to the TMS [53].

One additional output calculated by the full model is the total conversion efficiency:

$$\eta_{\text{tot}} = \begin{cases}
\frac{\sum_{i=0}^{n_{\text{EF}}} P_{\text{fan}_i}}{\text{LHV} \sum_{i=0}^{n_{\text{TG}}} \dot{m}_{fi} + n_p n_s P_{\text{cell}}} & P_{\text{cell}} \ge 0 \\
\frac{\sum_{i=0}^{n_{\text{EF}}} P_{\text{fan}_i} - n_p n_s P_{\text{cell}}}{\text{LHV} \sum_{i=0}^{n_{\text{TG}}} \dot{m}_{fi}} & P_{\text{cell}} < 0
\end{cases}$$
(18)

where LHV is the lower heating value of the jet fuel (43.1 MJ/kg). This output is important to evaluate the system-level performance and behavior.

#### E. Model Validation

The model in the turboelectric configuration (without the BESS) was validated against a high-fidelity model of the aircraft [47]. The error on cumulative fuel burn over a 550 km mission profile is 0.88% and increases to 3.67% for the 1850 km mission because the variable is given by the integration of the fuel mass flow rate. Other variables were verified against the high-fidelity model, such as the FPT power, the fan power, and thrust with the root mean squares of the error of 0.03, 0.07, and 0.05%, respectively [19].

# IV. Design Space Exploration

The goal of the design space exploration (DSE) is to investigate the effects of the battery pack design on the fuel burn and on the optimal control strategy over different mission profile lengths. The airframe and turbomachinery considered in this study are designed and sized for the nominal mission of 1980 n miles and a total maximum takeoff weight of 33,991 kg for the case of pure turboelectricity (no batteries), as described in Ref. [47]. The hybrid configuration is here considered for shorter missions, when the maximum takeoff weight is

not reached and reconfigurable battery modules can be introduced to the floor of the aircraft. For this DSE, the airframe design is constrained and only the BESS size and cell chemistry are varied. Different mission profiles are then evaluated.

In addition, to evaluate the effect of battery temperature and cooling, the simulations are run by considering at first a constant battery temperature and then introducing a variable temperature. In the design exploration study, the battery total voltage is fixed by the maximum operating voltage of the bus (2 kV), which determines (with the cell chemistry) the number of cells in series in the battery pack. One variable considered in the DSE is the BESS mass because it directly affects the operation of the aircraft. The number of cells in parallel is then determined based on the dc bus voltage and the  $m_{\rm BESS}$  and  $m_{\rm cell}$ . The packaging factor  $f_p$  is introduced to account for the additional weight resulting from the connectors, wiring, thermal management, and enclosures:

$$m_{\rm BESS} = m_{\rm cell} n_p n_s f_p + m_{\rm conv} \tag{19}$$

where the  $f_p$  is assumed to be 1.25. The other variable considered in this study is the cell chemistry, which affects the specific power and energy of the BESS and, ultimately, the total energy carried on board. The DSE is conducted for three different missions to evaluate how the traveling distance affects the design and performance of the BESS. The BESS size is varied between 1000 kg and a maximum value determined by  $m_{\rm MTOW}$ , as described in Sec. III.A, whereas the cell characteristics and mission profiles are described in the following subsections. The maximum BESS mass is 5750 kg for mission A, 5000 kg for mission B, and 4000 kg for mission C.

The outputs of the study, which will be analyzed in the following sections, are the fuel burn, the optimal control strategy, the cooling power and efficiency, and the fuel savings. The fuel savings are calculated using the fuel burn of the equivalent fully turboelectric propulsion configuration. The reference aircraft is described in Sec. II, with the difference that, in the fully turboelectric configuration, the battery is not present [47]. The study consider savings only in terms of fuel burn. However, a fleet analysis that focuses on energy savings for the same aircraft was described in Ref. [54].

#### A. Cell Selection

The cells selected for the study are summarized in Table 1 and referred to as cells 1–6, respectively. All cells have been characterized experimentally at The Ohio State University; and the battery ECM [Eqs. (13–16)] was calibrated to the data collected. Cells 1–3 are commercially available, whereas cells 4–6 have a technology readiness levels (TRLs) below four and are only available as prototypes. Different than for parallel hybrid systems, which require high specific power cells, the series-parallel configuration is expected to achieve higher benefits with batteries having a higher specific energy [10]. For this reason, the cells were selected to cover

different combinations of specific energy and power by considering a minimum specific energy of  $200 \text{ (W} \cdot \text{h)/kg}$ . Cell selection ranges from a higher specific power cell (cell 1) to a high specific energy cell (cell 6).

The commercially available candidates were selected from an initial set of candidate technologies based on conducting multirate static and dynamic tests, as well as by comparing their performances. These cells were then put through the same tests at multiple temperatures to complete the characterization process. Cells 1–3 provided the lowest cell-to-cell variation. Having low TRLs, cells 4–6 were limited to room-temperature testing, with relatively low C-rate static and dynamic tests. As an example of the data used in the model, the full characterization of cell 1 is shown in Fig. 3. The voltage, current, and temperature limits are provided by the manufacturer; whereas the power limits are calculated using the voltage limits specified by the manufacturer. The cell heat capacity was experimentally derived at the cell level, whereas the value at the pack level was found in the literature for a battery pack made of cylindrical cells [49]. Additional details on the model can be found in Ref. [19].

# B. Mission Profiles

The missions used in the design space exploration include ranges of approximately 550, 1100, and 1850 km; and they are denoted as missions A, B, and C, respectively. All missions are characterized by a 0.8 Mach number and a 9100 m altitude during cruise, and they are shown in Fig. 4. These mission profiles have been determined during the sizing of the aircraft and were described in Ref. [47]. The profiles do not explicitly include takeoff or landing rolls but, rather, begin in initial climb and end in approach. This approach is followed because the takeoff and the landing rolls do not dramatically affect the control strategy (maximum engine power during climb and engine at idle during landing).

# C. Energy Management Strategy

The design space exploration of a hybrid power train requires assumptions on the energy management strategy. According to Refs. [36,55], this problem may be approached by formulating a nonlinear discrete optimal control problem and solving it via dynamic programming (DP) on a prescribed mission. DP was chosen because it provides the global optimal solution to the problem by evaluating all the feasible cases, even if it requires high computation power. The energy management strategy (EMS) aims at optimizing the following objective function:

$$J = \sum_{k=0}^{N} \dot{m}_{f, \text{tot}_k}(x_k, u_k)$$
 (20)

where  $u_k = [N_{1_k}, CR_k]$ . The problem is subject to the following state dynamics:

Table 1 Summary of cell manufacturer parameters and experimental characterization data

			Cell			
	1	2	3	4	5	6
Manufacturer	Sony	Kokam	Efest	OXIS	Zenlabs	OXIS
Model	US18650VTC6	SLPB065070180	IMR18650	POA000343	Glide	POA000412
Format	Cylinder	Pouch	Cylinder	Pouch	Pouch	Pouch
Chemistry	NMC	H-NMC	LMO	Li-S	Si	Li-S
Mass, g	47	173	47	140	131	85
Nominal capacity, Ah	3.0	12.0	3.5	19.5	12.7	16.0
Nominal voltage, V	3.6	3.7	3.7	2.15	3.7	2.15
Maximum voltage, V	4.2	4.2	4.2	2.6	4.47	2.6
Minimum voltage, V	2.5	2.7	2.5	1.9	2.5	1.9
Cont. dch. Rate, C-rate	5	2	2.85	3	1	1
Cont. ch. rate, C rate	1	1	1.14	0.2	1	0.2
Specific energy, (W · h)/kg	232	257	278	299	359	405
Specific power, W/kg	1159	513	794	898	359	405
Heat capacity (cell), $J/(kg \cdot K)$	1198	878	1198	878	878	878
Heat capacity (pack), $J/(kg \cdot K)$	1300	953	1300	953	953	953

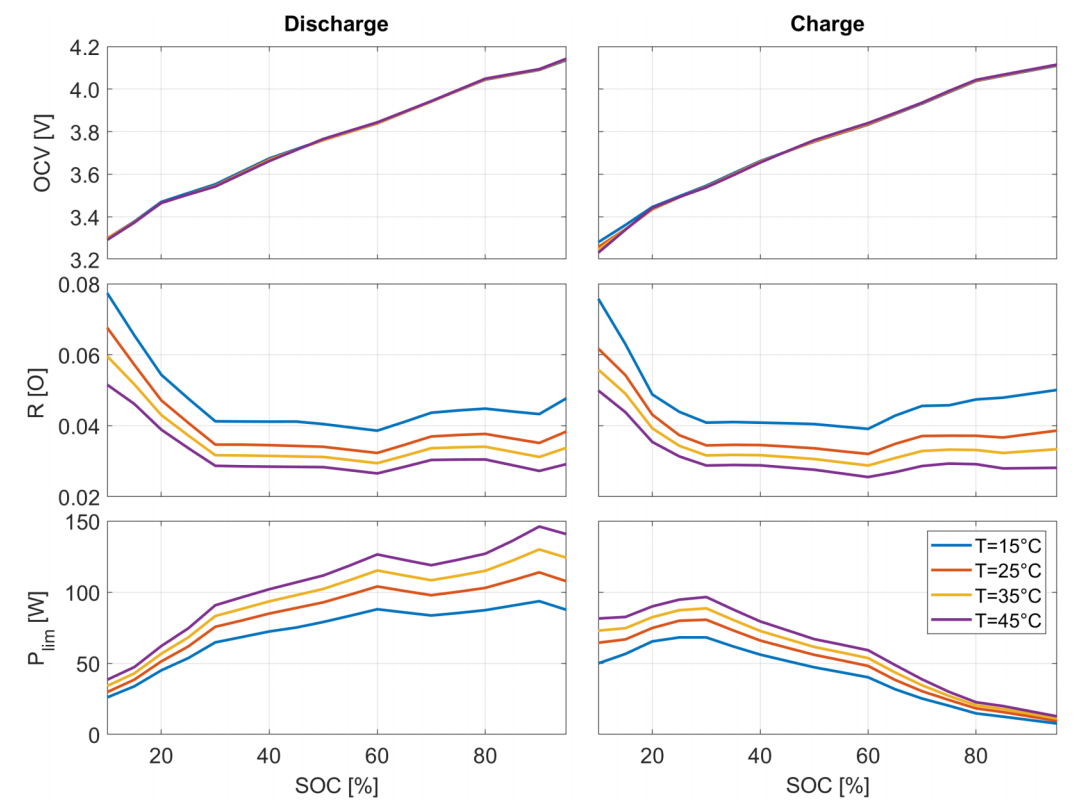


Fig. 3 SOC-, T- and mode-dependent parameters of the equivalent circuit model of cell 1.

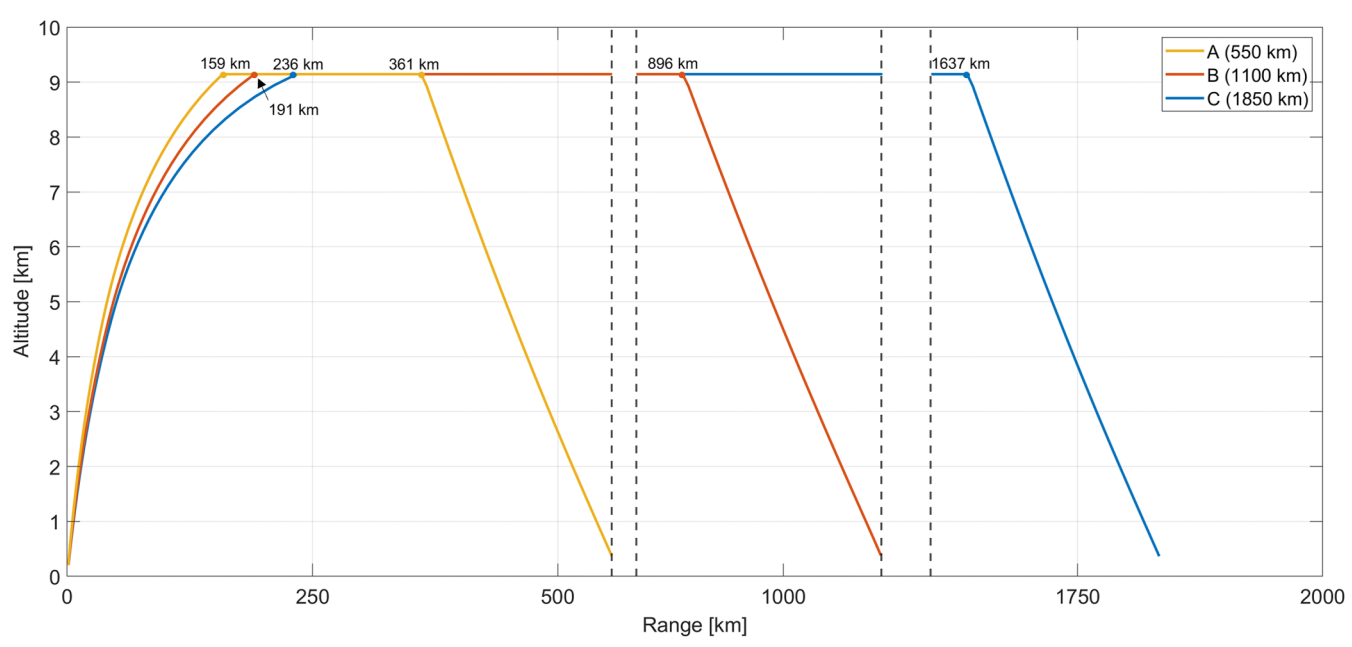


Fig. 4 Mission profiles considered in this analysis.

$$\begin{split} x_{k+1} &= \begin{bmatrix} \text{SOC}_{k+1} \\ T_{\text{BP}_{k+1}} \end{bmatrix} & \text{SOC}_{k} \in [10\%, 95\%] \\ &= \begin{bmatrix} \text{SOC}_{k} - \frac{I_{k}(x_{k}, u_{k})}{C_{\text{nom}}} \Delta t \\ T_{\text{BP}_{k}} + \frac{\dot{Q}_{\text{gen}}(x_{k}, u_{k}) - \dot{Q}_{\text{cool}}(x_{k}, u_{k})}{m_{\text{BP}}c_{\text{BP}}} \Delta t \end{bmatrix} \quad \forall \; k = 1, \dots, N \quad (21) \\ &N_{1_{k}} \in [45\%, 100\%] \end{split}$$

$$CR_k \in [0\%, 5\%]$$
 (25)

(22)

(23)

(24)

where  $\Delta t$  is 5 s. The problem is also subject to state and input constraints:

Note that, whereas  $N_1$  and the CR do not directly appear in Eqs. (20) and (21), they are present in the other model equations, such as

Eqs. (5) and (8). In addition, engine and fan feasible operating conditions and motor and power electronics and battery limitations are taken into account in the optimal control problem. The initial value of the SOC is 95%, which represent a fully charged battery; and the initial value of  $T_{\rm BP}$  is 23°C for all simulations. Note that in Eqs. (20) and (21), it is assumed that the total mass in the aircraft, which decreases during the mission, is not considered as a state. For the purpose of solving the optimal control problem, this assumption is consistent with the analysis shown in Ref. [19], which indicates a less than 0.5% error on the fuel burn. On the other hand, fuel mass affects the thrust request calculation, and therefore the performance of the aircraft. For this reason, an iterative process was adopted to estimate the initial value of the fuel mass and correct the results of the optimization [19].

To separate the effects of the SOC and the temperature on the EMS, the analysis focuses at first on simulations obtained with a constant battery temperature ( $T_{\rm BP}=23^{\circ}{\rm C}$ ) and cooling ratio (CR = 0%), and then on the comparison of results obtained with constant and variable battery temperatures and cooling ratios. Figure 5 shows the system and battery pack parameters for the different cell chemistries, which were obtained with a constant temperature over mission A. The high specific power and high-power limits of cell 1 allow for a different energy management strategy as compared to other cells. During climb, the battery power extracted is lower and the engine is used at higher-power levels, which increase the engine and system efficiency. When the mission profile switches to cruise and the power setting and efficiency decrease, the battery pack power increases to a high value to increase the efficiency of the system. Given that cell 1 is a lower specific energy cell as compared to the other cells, the highpower operation is maintained for a short time during cruise to avoid depleting the battery at the beginning of cruise. The lower power limits of cells 2 to 4 do not allow for this strategy, and hence the battery power extracted from the battery is approximately constant during the cruise phase. The behavior of cells 5 and 6 is similar to cells 2 to 4, with the exception that the 1 C current limits, as shown in Table 1, do not allow us to fully discharge the battery.

The introduction of the temperature and cooling ratio in the optimization affects the control strategy differently for different battery pack designs. It has been verified that considering a variable temperature does not affect the control strategy, in terms of battery electrical power, for cells 2 to 6; whereas it does affect the control strategy when considering cell 1. Figure 6 compares the values of the battery power, heat generation, cooling power, SOC, and temperature of the battery pack obtained in one case (blue lines) by setting the temperature and cooling ratio as constant in another case (orange lines) by optimizing the cooling ratio and tracking the temperature for cell 1 on the mission profile A. In the simulation with constant temperature, the battery pack is used at peak power in the initial phase of cruise to extract as much power as possible at high efficiency. In the simulation with a variable temperature, this behavior is not optimal. When the battery pack is discharged at high power, the heat generation increases. If the simulation includes the temperature, the benefit of high efficiency does not outweigh the penalty for cooling the battery; therefore, the energy management strategy changes. In this case, the battery pack is used more during climb and the power is approximately constant during cruise. Figure 6 also shows the thermal management strategy for the battery: the controller allows the battery temperature to rise to operate in a higher-efficiency range (battery resistance decreases with temperature); and when the temperature reaches the maximum value, the controller modulates the cooling power in a cyclic manner to keep the temperature of the battery below the maximum value.

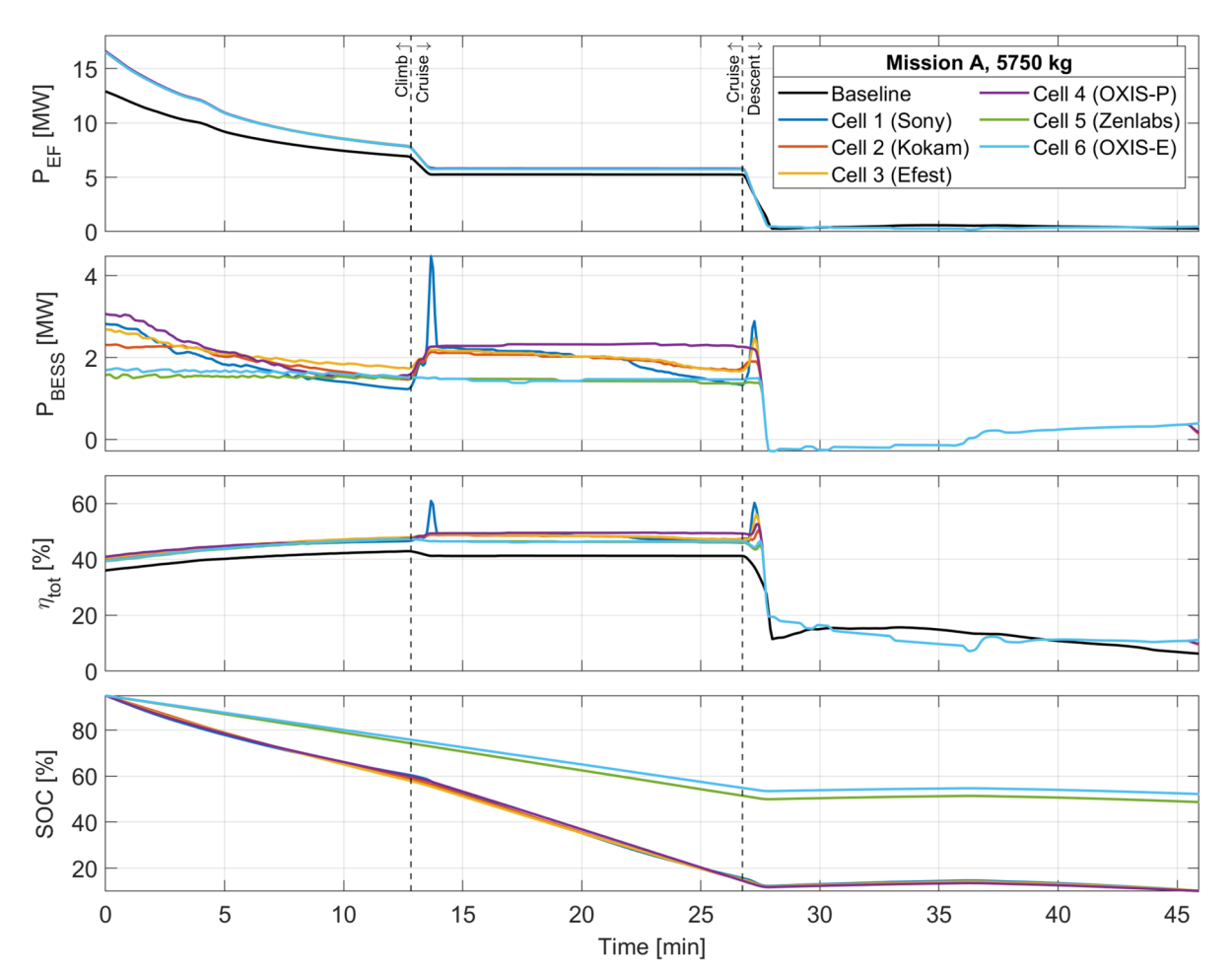


Fig. 5 Optimized system and battery pack performance throughout mission A with BESS size of 5750 kg ( $T_{\rm BP}=23^{\circ}{\rm C}$  and  ${\rm CR}=0\%$ ).

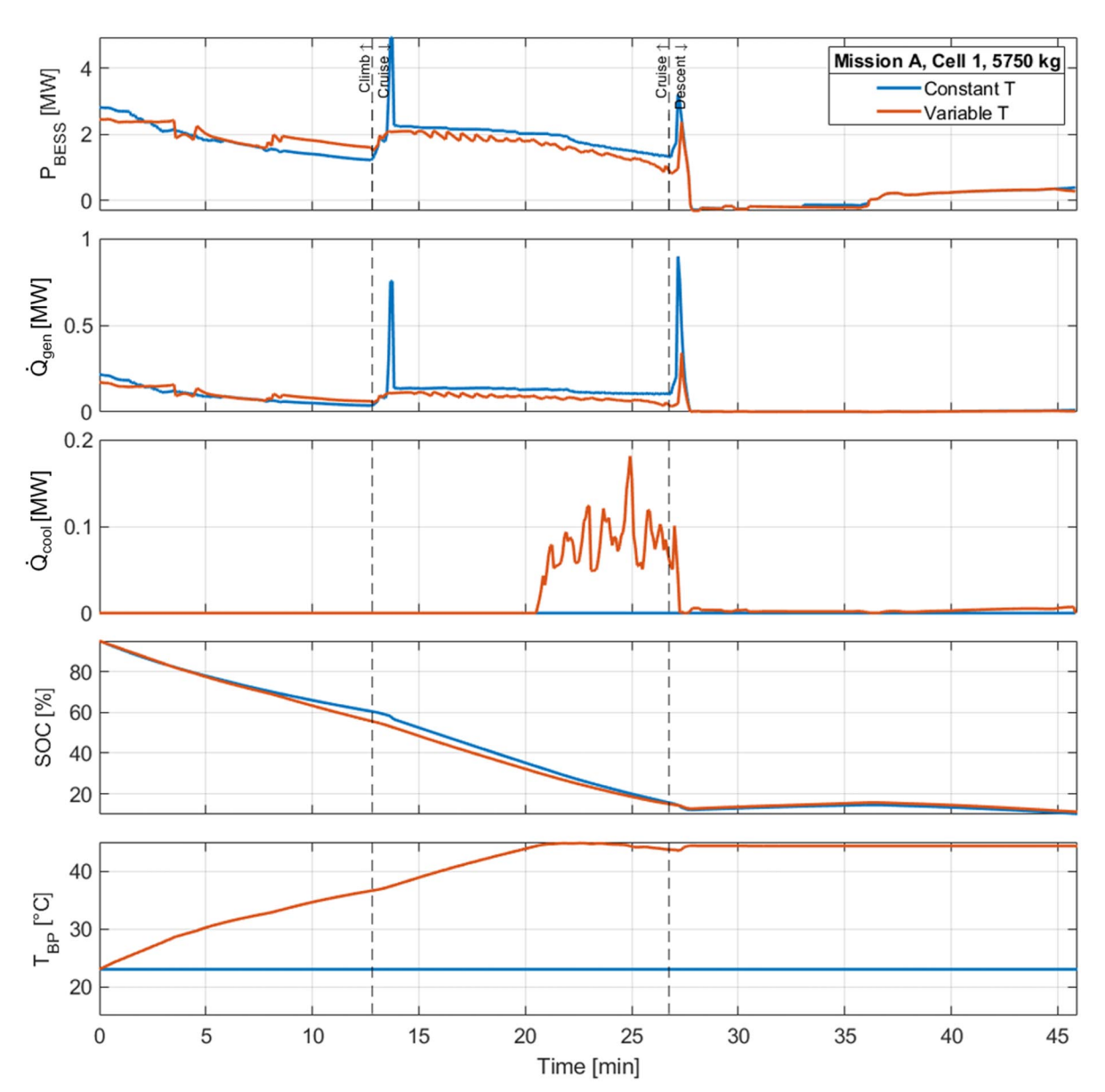


Fig. 6 Optimized system and battery pack performance for cell 1 throughout mission A with BESS size of 5750 kg.

# V. Results

The results show the effect of the DSE variables (battery pack design and mission profile) on fuel burn and fuel savings by considering constant temperature at first and then later on evaluating the effect of a variable temperature on fuel savings. The total number of cases for the DSE is 160 by considering three mission profiles, six cell chemistries, and up to seven battery pack size options. For the variable temperature analysis, only four cells (1, 2, 3, and 5) were considered because cells 4 and 6 could not be characterized experimentally at various temperatures because of their low TRLs. Figure 7 shows how the segment and overall fuel savings vary between different cell selections in missions A, B, and C with BESS sizes of 5750, 5000, and 4000 kg, respectively. This represents the maximum allowed size for each mission profile. All cells offer similar fuel savings in descent because of the low-power request from the electric fans. During climb and cruise, the fuel savings generally increase with specific energy, except for cells 5 and 6 on mission A. This limitation is given by the low current limits of these high specific energy cells. The current limits prevent the battery from discharging completely, reducing the fuel savings in both climb and cruise, as well as overall. When using cells with high specific power, the battery is capable of providing the majority of the electric fan power sooner in the descent segment, resulting in slightly higher fuel savings. On the other hand, it performs relatively poorly in climb and cruise because it reserves energy for descent and starts the mission with relatively low energy. In fact, the 5750 kg BESS comprising cell 1 is capable of 9.43 MW of power output versus 1.94 MW for a BESS comprising cell 6, but it has 0.94 MW  $\cdot$  h of available energy versus 1.55 MW  $\cdot$  h for a BESS comprising cell 6. In addition, high specific power cells are penalized by the need for a higher-power dc/dc converter, which limits the available mass for the cells, as demonstrated in Eq. (19).

With increasing mission range, battery use shifts toward the cruise and descent segments. Increasing the mission range primarily increases cruise duration, range, and consequently fuel consumption. Fuel savings are higher for cells 5 and 6 with increasing range as compared to the other cells because the discharge current limit no longer inhibits the battery from being fully discharged. Otherwise, as the range increases, fuel consumption increases; likewise, savings decrease because the overall energy expenditure begins to exceed the energy storage capability of the battery pack.

The spider charts presented in Fig. 8 compare the aggregate data for all cells and missions, with the BESS sized optimally for each case. As the mission range and baseline fuel consumption increase, the maximum allowable BESS size is reduced, regardless of cell selection. Thus, for all cells, the BESS size decreases with increasing range. Cells 3–6 have sufficient system-level specific energy to be sized at the maximum allowable size across all missions. The optimal

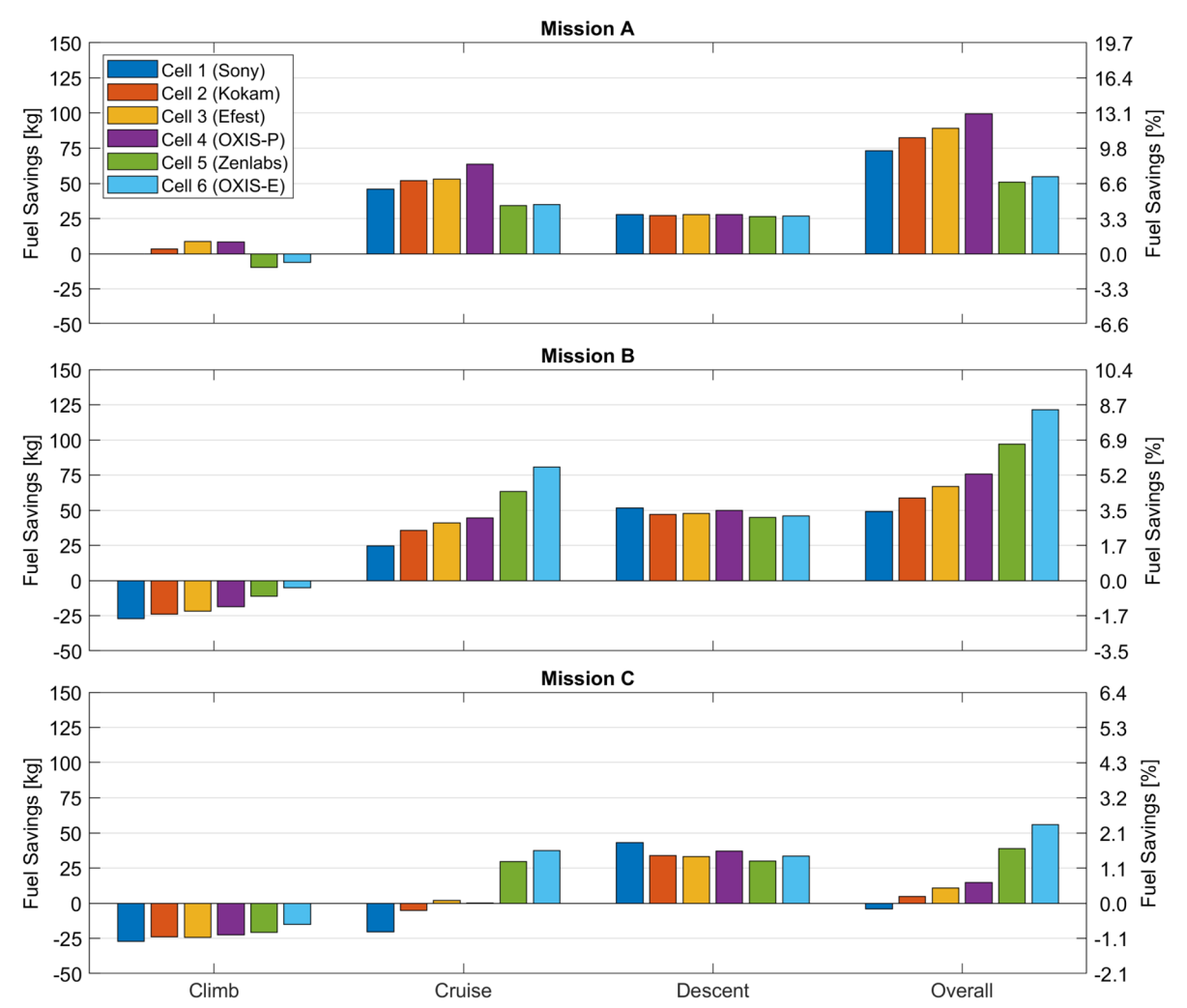


Fig. 7 Fuel burn reduction, relative to baseline nonhybrid system, as a function of cell, range, and segment for maximum allowable BESS size in each mission ( $T_{\rm BP} = 23^{\circ}$ C and CR = 0%) [47]. Figure data can be found in Table A3 in Appendix.

BESS size for mission C reduces progressively from cell 3 to cell 1 as the specific energy decreases. Generally, the fuel savings decrease with increasing mission range because the overall energy expenditure increases and energy storage capability decreases. Practically, the fuel savings are a function of the capacity removed from the battery, and the capacity is dependent on the sizing and specific energy. Lower specific energy results in lower energy stored for the same BESS size; and the dc/dc converter sizing compounds this effect because specific power generally increases with decreasing specific energy. In mission A, the battery packs using cells 4 and 6 have more installed capacity than those for missions B and C. However, current limits prevent the full capacity from being removed. These are the only instances where the energy extracted is not proportional to the BESS size.

Excluding current-limited cells, when comparing different cell chemistries for a battery pack of the same size on the same mission profile, the mean discharge power increases with increasing specific energy simply because more energy must be discharged in the same duration. Furthermore, the mean discharge rate is practically the same for every cell for a given mission. This is primarily due to the smoothness of the mission profiles. If the profile contained large variations in thrust request corresponding to steps in altitude changes, the battery pack would be discharged in pulses at differing magnitude and duration corresponding to the power capability of the battery pack. The mean heat generation is a function of mean discharge power (and charge power, which is negligible), cell internal resistance, and pack architecture. Cells 1 and 2 have equivalent mean discharge power and heat generation, whereas cell 2 exhibits one-third the internal resistance and has four times the capacity of cell 1.

The peak discharge power, discharge rate, and heat generation are most influenced by cell parameters and BESS size, otherwise having no dependence on mission range. The cell with the highest power and current limits (by unit mass), which is cell 1, exhibits the highest peak power and rate. Current and power limits can vary somewhat independently such that the relative scale of the peak discharge rate and power vary accordingly. Generally, these both decrease with increasing specific energy, whereas peak heat generation is additionally governed by internal resistance and voltage range.

Considering the same mission and BESS size, generally, fuel savings increase with the increase of cell specific energy. This assumes that cell limitations do not impair the BESS for a significant portion of the mission and neglect any differences in packaging efficiency between cells of different form factors. For example, Fig. 9 shows the two most energy-dense cells suffer in performance in mission A because the durations of the mission and current limits prevent the battery from being fully discharged, whereas a cell with a specific power three times the specific energy provides higher benefits. In fact, shorter-range missions require highly power-dense cells, or cells with higher allowable discharge current. Still, increasing the size of the BESS using cells 5 and 6, along with all other cells, reduces fuel consumption because of relatively low overall energy use. For longer-range missions, the fuel savings decrease dramatically to a value between 0 and 2% for mission C. These solutions may not be considered attractive for industry applications.

Cell 4 provides the best benefits for mission A and cell 6 for missions B and C. It is important to note that these cells are prototypes, and are therefore not commercially available. This impacts the cost, availability, and safety of the cells, which have to be taken into

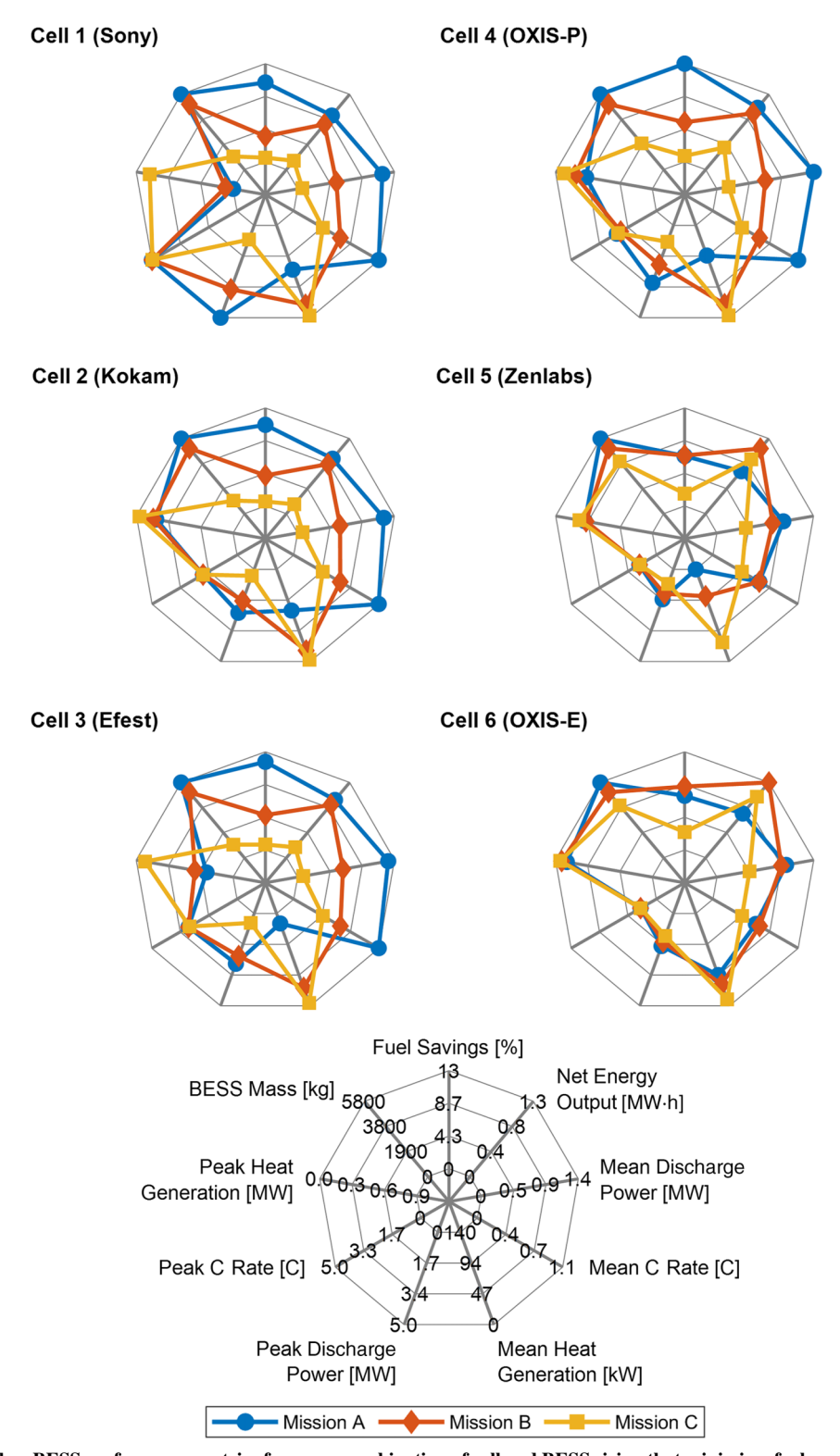


Fig. 8 Comparison of key BESS performance metrics for every combination of cell and BESS sizing that minimizes fuel consumption in each mission  $(T_{\rm BP}=23^{\circ}{\rm C})$  and  $(T_{\rm BP}=23^{\circ}{\rm C})$ . Figure data can be found in Table A3 in Appendix.

consideration during the feasibility study for the aircraft. For example, for mission A, it might be more convenient from a cost perspective to select cell 3 instead of cell 4, reducing the fuel savings by less than 2% but moving to a commercially available cell.

The effects of tracking the temperature and controlling the cooling power are negligible on longer mission profiles because the average battery power levels are lower, reducing the heat generation in the battery pack, but this is relevant in the shortest mission profile (mission A). Figure 10 shows the fuel savings for four different cell chemistries. Generally, the introduction of battery cooling increases

the fuel burn, reducing the fuel savings. However, for cell 2 in the case of the smallest battery pack size, the introduction of tracking the temperature and controlling the cooling power provide a benefit: the heat generation for the smaller battery pack is lower and the EMS can take advantage of operating the battery in higher-efficiency conditions. The difference between fuel savings with constant and variable temperatures is determined by the amount of heat generated by the battery. For batteries with low heat generation, such as cell 1, the differences are negligible; whereas for batteries with high heat generation, such as cells 3 and 5, they are not. In these conditions, the

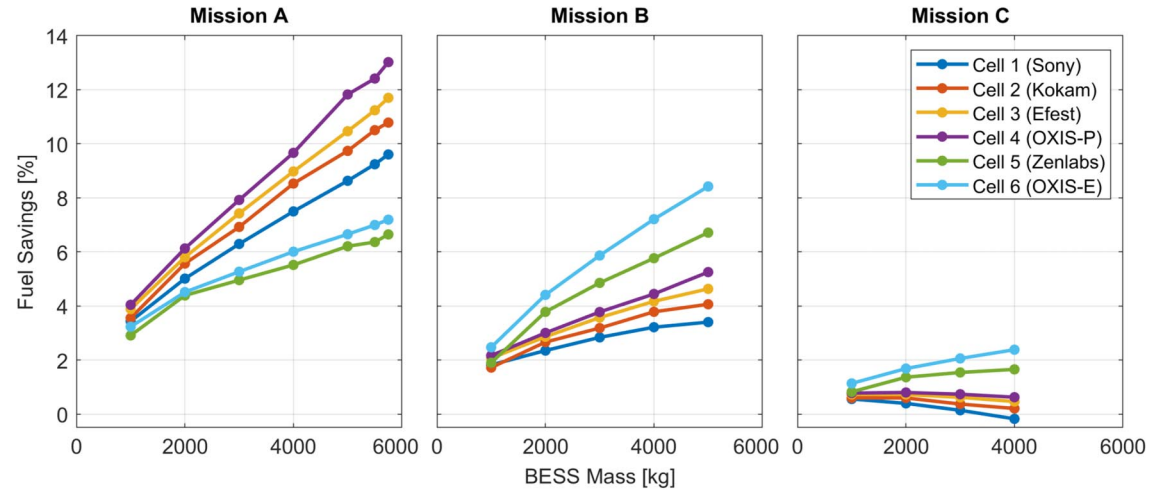


Fig. 9 Total fuel savings by cell selection, BESS size, and mission range ( $T_{\rm BP}=23^{\circ}{\rm C}$  and  ${\rm CR}=0\%$ ).

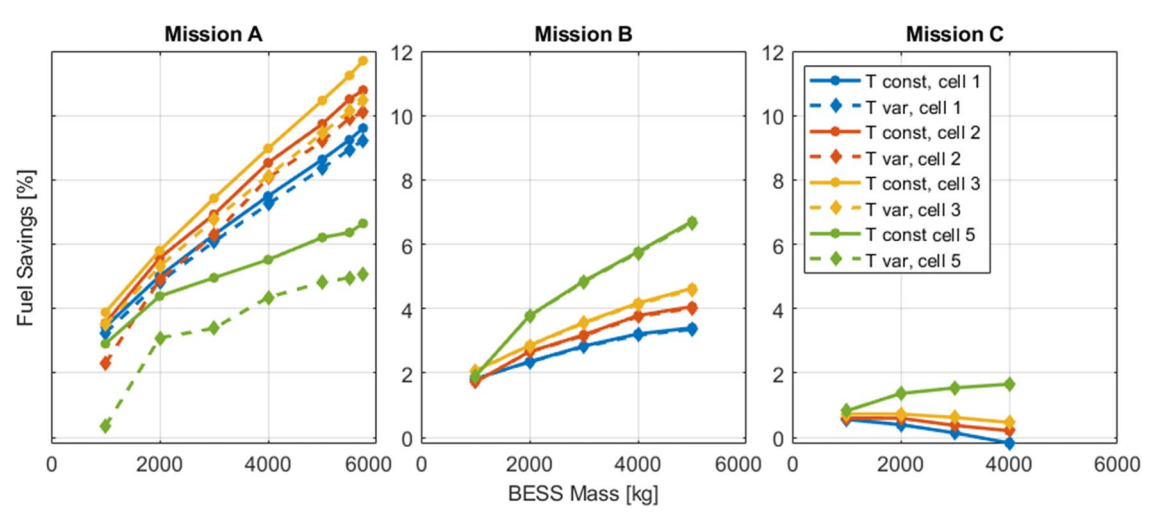


Fig. 10 Comparison of total fuel savings obtained with constant (const) battery temperature vs variable (var) battery temperature.

battery has to be cooled to operate in the temperature limits, guaranteeing correct operation of the battery and reducing degradation due to high-temperature operation.

#### VI. Conclusions

The dependencies of fuel burn and energy management on cell characteristics, BESS sizing, and mission range were evaluated. Six cell models (three state-of-the-art and three future technologies), discrete BESS masses (up to the maximum mass), and three mission ranges (ranges between 550 and 1850 km) were considered. The results of the study indicate the interdependence of the power split control strategy and thermal management strategy with the cell technology selection and design of the battery pack. As expected, fuel savings increase with decreasing mission range or increasing BESS size, with one exception for batteries with relatively low specific energy. Furthermore, fuel savings increase as the cell specific energy increases, unless the battery pack is current limited and in a short-duration mission. In descent, the engine control most significantly deviates from the baseline because of the low-power operation. Otherwise, the power split is relatively constant in climb and cruise. With increasing mission range, a larger percent of stored energy is used in cruise; and the mean discharge power, mean discharge rate, and mean heat generation decrease. Similar trends are observed with decreasing the BESS size. Additionally, the peak discharge power, peak discharge rate, and peak heat generation decrease. Overall, the highest fuel savings for shorter mission ranges are obtained with high specific power cells combined with a specific energy above 250  $(W \cdot h)/kg$ ; whereas on longer missions, a high specific energy cell provides the best benefits.

Introducing the temperature as a state and the cooling ratio as a control input in the optimization has an effect on both the optimal energy management strategy and the fuel burn. For high specific power cells, such as cell 1, the profile of the power extracted from the battery is smoother, with no drastic changes in power levels, because high power generates high heat, which then needs to be dissipated. For more balanced cells, from an energy and specific power perspective, the power profile is less affected by the introduction of the temperature in the optimization. Fuel savings are affected by the cooling power in the case of high heat generation, which is influenced by the cell chemistry and by the length of the mission profile. For longer mission profiles, the effects of the temperature and battery cooling are negligible.

# **Appendix: System Parameters and Numerical Results**

Table A1 lists the values of the parameters used in the simulations. The data come from the work described in Refs. [47,48,51].

Table A2 list the values of the fuel savings for all cells and mission, which are divided into the three mission segments and shown in Fig. 7.

Table A3 lists the values of the battery variables for all cells and missions, which are shown in Fig. 8.

Table A1 System and component parameter values

Parameter	Description	Measurement unit	Value	
	Vehicle			
$m_{\mathrm{MTOW}}$	Maximum mass for takeoff	kg	34,000	
$m_e$	Mass of empty aircraft and crew	kg	23,200	
$m_p$	Payload mass	kg	3,700	
	Electric fan			
$P_{\mathrm{des}_{\mathrm{EM}}}$	Motor design power	MW	2.1	
$\eta_{\mathrm{EM}}$	Motor efficiency	%	97.5	
$\eta_{\mathrm{inv}}$	Inverter efficiency	%	98.3	
	Turbogenerator			
$P_{ m des_{gen}}$	Generator design power	MW	4.5	
$\eta_{ m gen}$	Generator efficiency	%	97.5	
$\eta_{ m rec}$	Rectifier efficiency	%	98.3	
LHV	Fuel lower heating value	MJ/kg	43.1	
	BESS			
$\eta_{ m conv}$	Dc/dc converter efficiency	%	98.3	

Table A2 Fuel savings for each mission segment represented in Fig. 7

		Cli	mb	Crı	Cruise		Descent		erall
Mission	Cell	kg	%	kg	%	kg	%	kg	%
A	1	-0.2	0.03	45.9	6.02	27.9	3.65	73.3	9.61
	2	3.5	0.46	52.0	6.81	27.2	3.57	82.3	10.79
	3	8.6	1.13	53.2	6.97	27.9	3.66	89.3	11.70
	4	8.2	1.08	63.7	8.34	28.0	3.67	99.4	13.02
	5	-9.6	-1.26	34.3	4.49	26.4	3.46	50.7	6.65
	6	-6.2	-0.81	34.8	4.55	26.6	3.49	54.9	7.19
В	1	-27.2	-1.88	24.8	1.72	51.5	3.56	49.1	3.40
	2	-23.9	-1.65	35.6	2.47	46.8	3.24	58.7	4.06
	3	-21.8	-1.51	41.0	2.84	47.8	3.31	66.9	4.63
	4	-18.6	-1.29	44.6	3.09	49.9	3.46	75.9	5.25
	5	-11.2	-0.78	63.4	4.39	44.9	3.11	97.0	6.71
	6	-5.0	-0.35	80.7	5.59	46.0	3.19	121.6	8.42
C	1	-27.0	-1.15	-20.2	-0.86	43.0	1.84	-4.1	-0.18
	2	-23.8	-1.02	-5.2	-0.22	33.8	1.44	4.9	0.21
	3	-24.3	-1.04	1.9	0.08	33.2	1.42	10.9	0.46
	4	-22.6	-0.96	0.0	0.00	37.1	1.59	14.6	0.62
	5	-20.9	-0.89	29.6	1.26	30.1	1.28	38.7	1.65
	6	-15.1	-0.64	37.5	1.60	33.4	1.43	55.8	2.38

# Acknowledgment

The authors thank the NASA University Led Initiative program titled "Electric Propulsion: Challenges and Opportunities" for sponsoring this research (grant: NNX17AJ92A).

#### References

- [1] Lee, D. S., Pitari, G., Grewe, V., Gierens, K., Penner, J. E., Petzold, A., Prather, M. J., Schumann, U., Bais, A., Berntsen, T., Iachetti, D., Lim, L. L., and Sausen, R., "Transport Impacts on Atmosphere and Climate: Aviation," *Atmospheric Environment*, Vol. 44, No. 37, 2010, pp. 4678– 4734.
- https://doi.org/10.1016/j.atmosenv.2009.06.005
  [2] Yim, S. H. L., Lee, G. L., Lee, I. H., Allroggen, F., Ashok, A., Caiazzo, F., Eastham, S. D., Malina, R., and Barrett, S. R. H., "Global, Regional and Local Health Impacts of Civil Aviation Emissions," *Environmental Research Letters*, Vol. 10, No. 3, 2015, Paper 034001.
- https://doi.org/10.1088/1748-9326/10/3/034001
  [3] Grobler, C., Wolfe, P. J., Dasadhikari, K., Dedoussi, I. C., Allroggen, F., Speth, R. L., Eastham, S. D., Agarwal, A., Staples, M. D., Sabnis, J., and Barrett, S. R. H., "Marginal Climate and Air Quality Costs of Aviation Emissions," *Environmental Research Letters*, Vol. 14, No. 11, 2019, Paper 114031. https://doi.org/10.1088/1748-9326/ab4942
- [4] Epstein, A. H., and O'Flarity, S. M., "Considerations for Reducing Aviation's CO2 with Aircraft Electric Propulsion," *Journal of Propul*sion and Power, Vol. 35, No. 3, 2019, pp. 572–582. https://doi.org/10.2514/1.B37015
- [5] Rosero, J. A., Ortega, J. A., Aldabas, E., and Romeral, L., "Moving Towards a More Electric Aircraft," *IEEE Aerospace and Electronic Systems Magazine*, Vol. 22, No. 3, 2007, pp. 3–9. https://doi.org/10.1109/MAES.2007.340500
- [6] Sarlioglu, B., and Morris, C. T., "More Electric Aircraft: Review, Challenges, and Opportunities for Commercial Transport Aircraft," *IEEE Transactions on Transportation Electrification*, Vol. 1, No. 1, 2015, pp. 54–64. https://doi.org/10.1109/TTE.2015.2426499
- [7] Wheeler, P., and Bozhko, S., "The More Electric Aircraft: Technology and Challenges," *IEEE Electrification Magazine*, Vol. 2, No. 4, 2014, pp. 6–12. https://doi.org/10.1109/MELE.2014.2360720
- [8] Friedrich, C., and Robertson, P., "Hybrid-Electric Propulsion for Aircraft," *Journal of Aircraft*, Vol. 52, No. 1, 2015, pp. 176–189. https://doi.org/10.2514/1.C032660
- [9] Biser, S., Filipenko, M., Boll, M., Kastner, N., Atanasov, G., Hepperle, M., Keller, D., Vechtel, D., and Noe, M., "Design Space Exploration Study and Optimization of a Distributed Turbo-Electric Propulsion System for a Regional Passenger Aircraft," AIAA Propulsion and Energy 2020 Forum, AIAA Paper 2020-3592, 2020. https://doi.org/10.2514/6.2020-3592

Table A3 Battery maximum and mean operating conditions, shown in Fig. 8 data

Cell	Mission	Fuel saving, %	Energy out, kW · h	Average discharge power, kW	Average <i>Cr</i> , C	Average heat generation, kW	Peak discharge power, kW	Peak <i>Cr</i> , C	Peak heat generation, kW	BESS mass, kg
1	Α	9.61	910.81	1190.17	1.11	73.64	5026.54	4.99	897.62	5750
	В	3.40	762.87	545.45	0.61	19.82	3479.22	4.98	825.74	5000
	C	0.56	148.58	66.28	0.38	3.07	771.46	4.96	124.81	1000
2	A	10.79	929.00	1213.94	1.11	78.28	2364.92	2.00	183.52	5750
	В	4.06	837.12	598.53	0.61	16.89	1719.14	2.00	155.32	5000
	C	0.60	158.66	70.78	0.38	2.75	349.43	2.00	28.24	1000
3	A	11.70	974.46	1273.34	1.11	126.23	2735.85	2.84	651.28	5750
	В	4.63	890.92	637.00	0.61	27.46	2316.90	2.84	543.48	5000
	C	0.73	176.32	78.65	0.38	4.33	509.17	2.79	81.54	1000
4	A	13.02	1041.85	1361.40	1.11	95.21	3127.73	2.31	284.08	5750
	В	5.25	950.17	679.37	0.61	20.63	2140.83	2.09	181.64	5000
	C	0.80	371.80	165.86	0.38	3.54	895.41	2.24	78.07	2000
5	Α	6.65	716.29	935.98	0.60	141.42	1629.06	1.00	270.87	5750
	В	6.71	1100.77	787.04	0.60	100.25	1329.01	0.98	281.74	5000
	C	1.65	917.35	409.22	0.38	29.44	794.32	0.97	220.13	4000
6	A	7.19	744.28	972.57	0.56	47.14	1771.40	0.92	105.28	5750
	В	8.42	1268.57	907.02	0.61	32.66	1535.27	0.92	57.46	5000
	C	2.38	1028.49	458.81	0.38	9.88	1220.76	0.92	43.18	4000

[10] Finger, D. F., Braun, C., and Bil, C., "Comparative Assessment of Parallel-Hybrid-Electric Propulsion Systems for Four Different Aircraft," *Journal of Aircraft*, Vol. 57, No. 5, 2020, pp. 843–853. https://doi.org/10.2514/1.C035897

- [11] Jones, C. E., Norman, P. J., Galloway, S. J., Armstrong, M. J., and Bollman, A. M., "Comparison of Candidate Architectures for Future Distributed Propulsion Aircraft," *IEEE Transactions on Applied Super*conductivity, Vol. 26, No. 6, 2016, pp. 1–9. https://doi.org/10.1109/TASC.2016.2530696
- [12] Berg, F., Palmer, J., Miller, P., Husband, M., and Dodds, G., "HTS Electrical System for a Distributed Propulsion Aircraft," *IEEE Transactions on Applied Superconductivity*, Vol. 25, No. 3, 2015, pp. 1–5. https://doi.org/10.1109/TASC.2014.2384731
- [13] Gohardani, A. S., Doulgeris, G., and Singh, R., "Challenges of Future Aircraft Propulsion: A Review of Distributed Propulsion Technology and Its Potential Application for the All Electric Commercial Aircraft," *Progress in Aerospace Sciences*, Vol. 47, No. 5, 2011, pp. 369–391. https://doi.org/10.1016/j.paerosci.2010.09.001
- [14] de Vries, R., Brown, M., and Vos, R., "Preliminary Sizing Method for Hybrid-Electric Distributed-Propulsion Aircraft," *Journal of Aircraft*, Vol. 56, No. 6, 2019, pp. 2172–2188. https://doi.org/10.2514/1.C035388
- [15] Pornet, C., and Isikveren, A. T., "Conceptual Design of Hybrid-Electric Transport Aircraft," *Progress in Aerospace Sciences*, Vol. 79, Nov. 2015, pp. 114–135. https://doi.org/10.1016/j.paerosci.2015.09.002
- [16] Pornet, C., Gologan, C., Vratny, P. C., Seitz, A., Schmitz, O., Isikveren, A. T., and Hornung, M., "Methodology for Sizing and Performance Assessment of Hybrid Energy Aircraft," *Journal of Aircraft*, Vol. 52, No. 1, 2015, pp. 341–352. https://doi.org/10.2514/1.C032716
- [17] Voskuijl, M., van Bogaert, J., and Rao, A. G., "Analysis and Design of Hybrid Electric Regional Turboprop Aircraft," CEAS Aeronautical Journal, Vol. 9, No. 1, 2018, pp. 15–25. https://doi.org/10.1007/s13272-017-0272-1
- [18] Sgueglia, A., Schmollgruber, P., Bartoli, N., Benard, E., Morlier, J., Jasa, J., Martins, J. R. R. A., Hwang, J. T., and Gray, J. S., "Multidisciplinary Design Optimization Framework with Coupled Derivative Computation for Hybrid Aircraft," *Journal of Aircraft*, Vol. 57, No. 4, 2020, pp. 715–729. https://doi.org/10.2514/1.C035509
- [19] Sergent, A., Ramunno, M., D'Arpino, M., Canova, M., and Perullo, C., "Optimal Sizing and Control of Battery Energy Storage Systems for Hybrid Turboelectric Aircraft," SAE International Journal of Advances and Current Practices in Mobility, Vol. 2, No. 3, 2020, pp. 1266–1278. https://doi.org/10.4271/2020-01-0050
- [20] El-Refaie, A., and Osama, M., "High Specific Power Electrical Machines: A System Perspective," CES Transactions on Electrical Machines and Systems, Vol. 3, No. 1, 2019, pp. 88–93. https://doi.org/10.30941/CESTEMS.2019.00012
- [21] Sziroczak, D., Jankovics, I., Gal, I., and Rohacs, D., "Conceptual Design of Small Aircraft with Hybrid-Electric Propulsion Systems," *Energy*, Vol. 204, Aug. 2020, Paper 117937. https://doi.org/10.1016/j.energy.2020.117937
- [22] Riboldi, C. E., "An Optimal Approach to the Preliminary Design of Small Hybrid-Electric Aircraft," *Aerospace Science and Technology*, Vol. 81, Oct. 2018, pp. 14–31. https://doi.org/10.1016/j.ast.2018.07.042
- [23] Finger, D. F., Bil, C., and Braun, C., "Initial Sizing Methodology for Hybrid-Electric General Aviation Aircraft," *Journal of Aircraft*, Vol. 57, No. 2, 2020, pp. 245–255. https://doi.org/10.2514/1.C035428
- [24] Swanke, J., Bobba, D., Jahns, T. M., and Sarlioglu, B., "Comparison of Modular PM Propulsion Machines for High Power Density," 2019 IEEE Transportation Electrification Conference and Expo (ITEC), IEEE Publ., Piscataway, NJ, 2019, pp. 1–7. https://doi.org/10.1109/ITEC.2019.8790587
- [25] Sirimanna, S., Thanatheepan, B., Lee, D., Agrawal, S., Yu, Y., Wang, Y., Anderson, A., Banerjee, A., and Haran, K., "Comparison of Electrified Aircraft Propulsion Drive Systems with Different Electric Motor Topologies," *Journal of Propulsion and Power*, Vol. 37, No. 5, 2021, pp. 733–747. https://doi.org/10.2514/1.B38195
- [26] Bodson, M., Sadey, D. J., Hunker, K. R., Theman, C. J., Taylor, L. M., and Csank, J. T., "Hybrid Electric Propulsion Using Doubly Fed Induction Machines," *Journal of Propulsion and Power*, Vol. 36, No. 1, 2020, pp. 78–87. https://doi.org/10.2514/1.B37415

- [27] You, H., Wei, Z., Hu, B., Zhao, Z., Na, R., and Wang, J., "Partial Discharge Behaviors in Power Modules Under Square Pulses with Ultrafast dv/dt," *IEEE Transactions on Power Electronics*, Vol. 36, No. 3, 2021, pp. 2611–2620. https://doi.org/10.1109/TPEL.2020.3014043
- [28] Deisenroth, D. C., and Ohadi, M., "Thermal Management of High-Power Density Electric Motors for Electrification of Aviation and Beyond," *Energies*, Vol. 12, No. 19, 2019, p. 3594. https://doi.org/10.3390/en12193594
- [29] Bobba, D., Yao, Z., Swanke, J., Mandel, R., McCluskey, P., Jahns, T. M., and Sarlioglu, B., "Multi-Physics Based Analysis and Design of Stator Coil in High Power Density PMSM for Aircraft Propulsion Applications," AIAA Propulsion and Energy 2021 Forum, AIAA Paper 2021-3306, 2021. https://doi.org/10.2514/6.2021-3306
- [30] Abotsi, O. Y., and Kizito, J., "Numerical Study of Heat Transfer Augmentation in an Axially Rotating Pipe Equipped with Kenics Mixer," Case Studies in Thermal Engineering, Vol. 21, Oct. 2020, Paper 100695. https://doi.org/10.1016/j.csite.2020.100695
- [31] Abotsi, O. Y., and Kizito, J. P., "Turbulent heat Transfer Enhancement in an Axially Rotating Pipe Fitted with Kenics Segment Mixer," *Results in Engineering*, Vol. 7, Sept. 2020, Paper 100146. https://doi.org/10.1016/j.rineng.2020.100146
- [32] Nakka, S. K. S., and Alexander-Ramos, M. J., "Simultaneous Combined Optimal Design and Control Formulation for Aircraft Hybrid-Electric Propulsion Systems," *Journal of Aircraft*, Vol. 58, No. 1, 2021, pp. 53–62. https://doi.org/10.2514/1.C035678
- [33] D'Arpino, M., Cancian, M., Sergent, A., Canova, M., and Perullo, C., "A Simulation Tool for Turbo-Hybrid-Electric Aircraft Battery Life Prediction for the NASA ULI Program," AIAA Propulsion and Energy 2019 Forum, AIAA Paper 2019-4469, 2019. https://doi.org/10.2514/6.2019-4469
- [34] Wu, J., Zou, Y., Zhang, X., Liu, T., Kong, Z., and He, D., "An Online Correction Predictive EMS for a Hybrid Electric Tracked Vehicle Based on Dynamic Programming and Reinforcement Learning," *IEEE Access*, Vol. 7, July 2019, pp. 98,252–98,266. https://doi.org/10.1109/ACCESS.2019.2926203
- [35] Sun, C., Hu, X., Moura, S. J., and Sun, F., "Velocity Predictors for Predictive Energy Management in Hybrid Electric Vehicles," *IEEE Transactions on Control Systems Technology*, Vol. 23, No. 3, 2015, pp. 1197–1204. https://doi.org/10.1109/TCST.2014.2359176
- [36] Serrao, L., Onori, S., and Rizzoni, G., "A Comparative Analysis of Energy Management Strategies for Hybrid Electric Vehicles," *Journal of Dynamic Systems, Measurement, and Control*, Vol. 133, No. 3, 2011, Paper 031012. https://doi.org/10.1115/1.4003267
- [37] Sabri, M., Danapalasingam, K., and Rahmat, M., "A Review on Hybrid Electric Vehicles Architecture and Energy Management Strategies," *Renewable and Sustainable Energy Reviews*, Vol. 53, Jan. 2016, pp. 1433–1442. https://doi.org/10.1016/j.rser.2015.09.036
- [38] Perullo, C., Mavris, D., and Singh, R., "A Review of Hybrid-Electric Energy Management and Its Inclusion in Vehicle Sizing," *Aircraft Engineering and Aerospace Technology*, Vol. 86, No. 6, 2014, pp. 550–557. https://doi.org/10.1108/AEAT-04-2014-0041
- [39] Xie, Y., Savvarisal, A., Tsourdos, A., Zhang, D., and Gu, J., "Review of Hybrid Electric Powered Aircraft, Its Conceptual Design and Energy Management Methodologies," *Chinese Journal of Aeronautics*, Vol. 34, No. 4, 2021, pp. 432–450. https://doi.org/10.1016/j.cja.2020.07.017
- [40] Misley, A., D'Arpino, M., Ramesh, P., and Canova, M., "A Real-Time Energy Management Strategy for Hybrid Electric Aircraft Propulsion Systems," AIAA Propulsion and Energy 2021 Forum, AIAA Paper 2021-3283, 2021. https://doi.org/10.2514/6.2021-3283
- [41] Leite, J. P. S. P., and Voskuijl, M., "Optimal Energy Management for Hybrid-Electric Aircraft," Aircraft Engineering and Aerospace Technology, Vol. 92, No. 6, 2020, pp. 851–861. https://doi.org/10.1108/AEAT-03-2019-0046
- [42] Doff-Sotta, M., Cannon, M., and Bacic, M., "Optimal Energy Management for Hybrid Electric Aircraft," *IFAC-PapersOnLine*, Vol. 53, No. 2, 2020, pp. 6043–6049. https://doi.org/10.1016/j.ifacol.2020.12.1672
- [43] Wall, T. J., and Meyer, R. T., "Hybrid Electric Aircraft Switched Model Optimal Control," *Journal of Propulsion and Power*, Vol. 36, No. 4,

- 2020, pp. 488–497. https://doi.org/10.2514/1.B37419
- [44] Finger, D. F., Braun, C., and Bil, C., "Impact of Battery Performance on the Initial Sizing of Hybrid-Electric General Aviation Aircraft," *Journal* of Aerospace Engineering, Vol. 33, No. 3, 2020, Paper 04020007. https://doi.org/10.1061/(ASCE)AS.1943-5525.0001113
- [45] Hashemi, S. R., Bahadoran Baghbadorani, A., Esmaeeli, R., Mahajan, A., and Farhad, S., "Machine Learning-Based Model for Lithium-Ion Batteries in BMS of Electric/Hybrid Electric Aircraft," *International Journal of Energy Research*, Vol. 45, No. 4, 2021, pp. 5747–5765. https://doi.org/10.1002/er.6197
- [46] Geiss, I., and Voit-Nitschmann, R., "Sizing of the Energy Storage System of Hybrid-Electric Aircraft in General Aviation," CEAS Aeronautical Journal, Vol. 8, No. 1, 2017, pp. 53–65. https://doi.org/10.1007/s13272-016-0220-5
- [47] Perullo, C., Alahmad, A., Wen, J., D'Arpino, M., Canova, M., Mavris, D. N., and Benzakein, M. J., "Sizing and Performance Analysis of a Turbo-Hybrid-Electric Regional Jet for the NASA ULI Program," AIAA Propulsion and Energy 2019 Forum, AIAA Paper 2019-4490, 2019. https://doi.org/10.2514/6.2019-4490
- [48] Perullo, C., Shi, M., Cinar, G., Alahmad, A., Sanders, M., Mavris, D. N., and Benzakein, M. J., "An Update on Sizing and Performance Analysis of a Hybrid Turboelectric Regional Jet for the NASA ULI Program," AIAA Propulsion and Energy 2020 Forum, AIAA Paper 2020-3590, 2020. https://doi.org/10.2514/6.2020-3590
- [49] Shi, M., Sanders, M., Alahmad, A., Perullo, C., Cinar, G., and Mavris, D. N., "Design and Analysis of the Thermal Management System of a Hybrid Turboelectric Regional Jet for the NASA ULI Program," AIAA Propulsion and Energy 2020 Forum, AIAA Paper 2020-3572, 2020. https://doi.org/10.2514/6.2020-3572

[50] Perullo, C. A., Trawick, D. R., and Mavris, D. N., "Assessment of Engine and Vehicle Performance Using Integrated Hybrid-Electric Propulsion Models," *Journal of Propulsion and Power*, Vol. 32, No. 6, 2016, pp. 1305–1314. https://doi.org/10.2514/1.B35744

- [51] Swanke, J. A., Bobba, D., Jahns, T. M., and Sarlioglu, B., "Design of High-Speed Permanent Magnet Machine for Aerospace Propulsion," AIAA Propulsion and Energy 2019 Forum, AIAA Paper 2019-4483, 2019. https://doi.org/10.2514/6.2019-4483
- [52] Lyu, X., Tian, X., Li, H., You, H., and Wang, J., "Design of a Light-weight Low Inductance Power Module with Ceramic Baseplates," 2020 IEEE Applied Power Electronics Conference and Exposition (APEC), IEEE Publ., Piscataway, NJ, 2020, pp. 2782–2787. https://doi.org/10.1109/APEC39645.2020.9124073
- [53] Cai, Y., Cancian, M., D'Arpino, M., and Rizzoni, G., "A Generalized Equivalent Circuit Model for Large-Scale Battery Packs with Cell-to-Cell Variation," 2019 IEEE National Aerospace and Electronics Conference (NAECON), IEEE Publ., Piscataway, NJ, 2019, pp. 24–30. https://doi.org/10.1109/NAECON46414.2019.9057803
- [54] Shi, M., Cinar, G., and Mavris, D., "Fleet Analysis of a Hybrid Turboelectric Commercial Regional Jet under NASA ULI Program," AIAA Propulsion and Energy 2021 Forum, AIAA Paper 2021-3327, 2021. https://doi.org/10.2514/6.2021-3327
- [55] Sundström, O., Guzzella, L., and Soltic, P., "Optimal Hybridization in Two Parallel Hybrid Electric Vehicles Using Dynamic Programming," *IFAC Proceedings Volumes*, Vol. 41, No. 2, 2008, pp. 4642–4647. https://doi.org/10.3182/20080706-5-KR-1001.00781

G. Richards Associate Editor